Ground-state microwave-stimulated Raman transitions and adiabatic spin transfer in the ^{15}N nitrogen vacancy center

Florian Böhm,[1,2,*] Niko Nikolay,[1,2] Sascha Neinert,[1,2] Christoph E. Nebel,[3] and Oliver Benson[1,2]

[1]*Institut für Physik, Humboldt-Universität zu Berlin, Newtonstrasse 15, 12489 Berlin, Germany*

[2]*IRIS Adlershof, Humboldt-Universität zu Berlin, Zum Großen Windkanal 6, 12489 Berlin, Germany*

[3]*Nanomaterials Research Institute, Kanazawa University, Kanazawa, Ishikawa 920-1192, Japan*

(Received 25 March 2021; accepted 22 June 2021; published 2 July 2021)

Microwave pulse sequences are the basis of coherent manipulation of the electronic spin ground state in nitrogen vacancy (NV) centers. In this work we demonstrate stimulated Raman transitions (SRTs) and stimulated Raman adiabatic passage (STIRAP), two ways to drive the dipole-forbidden transition between two spin sublevels in the electronic triplet ground state of the NV center. This driving is achieved by a two-photon Raman microwave pulse which simultaneously drives two detuned transitions via a virtual level for SRTs or via two adiabatic and partially overlapping resonant microwave pulses for STIRAP. We lay the theoretical framework of SRT and STIRAP dynamics and verify experimentally the theoretical predictions of population inversion by observing the dipole-forbidden transition in the ground state of a single NV center. A comparison of the two schemes showed better robustness and success of the spin swap for STIRAP compared to SRT.

DOI: 10.1103/PhysRevB.104.035201

I. INTRODUCTION

Recent advances in coherent control techniques of individual electron spins in solid-state quantum systems have led to a broad spectrum of possible quantum technological applications [1]. Preparation and detection of quantum states mainly depend on the ability to reliably manipulate quantum systems effectively and coherently [2]. The simplest form of coherent control would be a two-level system (qubit) exposed to a weak resonant driving field, which leads to coherent Rabi oscillations between the two states. Either systems with multiple states can be effectively reduced to two-level systems by resonant control of individual transitions, or multiple states can be involved simultaneously by resonant or nonresonant control fields for extended coherent control of the system [3]. Moreover, instead of directly using the bare electronic states as a qubit, quantum information can be encoded in dressed states, which are generated by continuous driving of the quantum system [4]. This encoding can be desirable as dressed states offer coherence protection [5,6], for example, from bath-induced magnetic noise.

The nitrogen vacancy (NV) defect center in diamond [7,8] can be utilized as a model solid-state spin system which features multiple ground and excited states. The NV center forms a single localized quantum system, an electronic qutrit ground and excited state which can be coherently controlled at room temperature by microwave or laser pulses [9]. In addition, the state of the NV center can be optically prepared and read out in a convenient way, which makes it a very interesting and broadly studied solid-state spin system for a variety of quantum experiments such as quantum sensing [10–15], quantum information processing [16–18], and quantum computing [19,20]. Additionally, the nuclear spins associated with the NV center and its surrounding can be controlled as well. The latter often requires control of the employed isotope of the employed NV center [21].

This broad range of possible applications that the NV center offers stimulates great interest in developing further coherent control schemes or adapting already known control schemes to the NV center, for example, in the pursuit of enhancing magnetic field sensitivity [22–24].

Both optical and microwave fields can be utilized for coherent control. Here, we concentrate on microwave fields since they allow for better control of field amplitudes and phases and avoid spontaneous-emission decoherence [25]. Additionally, microwave antenna structures can easily be integrated in diamond optical chips. Finally, applying microwaves for quantum control of superconducting qubits has been established [26] at ultralow temperatures, which may render it advantageous for application with other diamond defect centers, such as the silicon vacancy center [27]. To gain more insight into the simultaneous control possibilities which the NV center offers we look into the application of microwave control schemes involving all three spin ground states of the NV center, the microwave stimulated Raman transition (SRT) and the stimulated adiabatic Raman passage (STIRAP). We adopt and establish the theoretical framework for SRT and STIRAP control in the ground state of the NV center and study these dynamics experimentally on a single NV center in ^{15}N δ-doped diamond. The STIRAP process is particularly interesting as it offers robustness against control pulse frequency and duration errors [28], and furthermore, an interrupted STIRAP process can be used to controllably dress and undress the NV states [4]. In contrast to previous works on optical Raman transitions in the NV center between two ground state spin

*Florian.Boehm@physik.hu-berlin.de

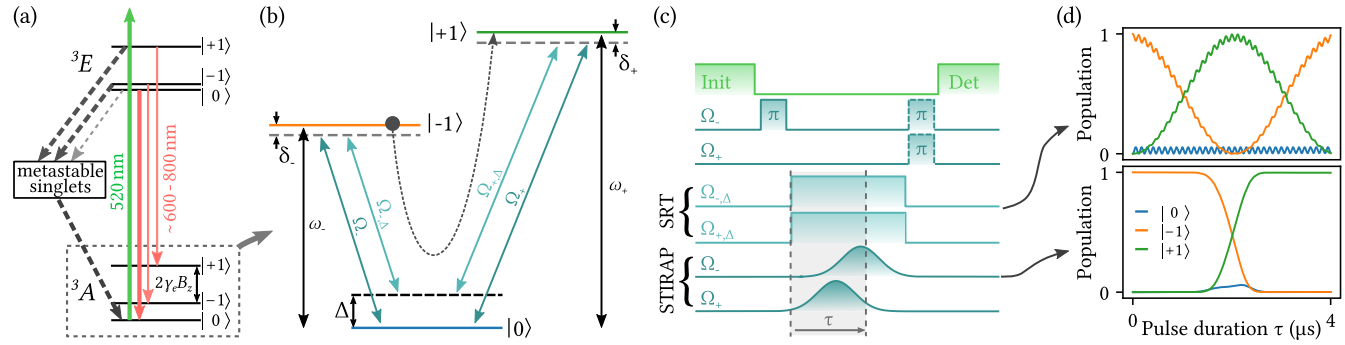

FIG. 1. Schematics for stimulated Raman transitions (SRTs) and stimulated Raman adiabatic passage (STIRAP). (a) Energy level diagram of the NV center (see main text). (b) NV spin triplet ground state with the transition energies and driving fields for SRTs and STIRAP. (c) Pulse sequence for SRTs and STIRAP. After polarizing the NV center into $|0\rangle$ with a green laser, the initial spin state is prepared with a resonant π_- pulse, swapping the population from $|0\rangle$ to $|-1\rangle$. Then the two Raman microwave pulses are applied for duration τ, either detuned by Δ from the resonant transition frequency to state $|0\rangle$ for SRTs or applied adiabatically and partially overlapping for STIRAP. Afterwards either the population in state $|0\rangle$ can directly be read out, or a $\pi_\pm$ pulse (shown by dashed lines) resonant to one of the two transitions is applied, swapping the population between $|\pm1\rangle \leftrightarrow |0\rangle$ to read out the population in $|+1\rangle$ or $|-1\rangle$. (d) Example dynamic evolution of the population of the three states $|0\rangle$ and $|\pm1\rangle$ as a function of the duration of two SRT or STIRAP pulses τ with color coding matching that in (b).

sublevels with an excited state [29,30] or microwave Raman transitions between synthetic Floquet levels [31], this work exploits the full spin-1 nature of the NV center, demonstrating full control of the dipole-forbidden transition between two spin sublevels via detuned or adiabatically overlapping microwave pulses.

The methods introduced in this work expand the already rich repertoire of control schemes for the NV center and could be an important ingredient for future quantum information, simulation, or sensing schemes using the NV center.

II. THEORETICAL FRAMEWORK

A single, negatively charged NV center's electronic spin ground state ^3A forms a triplet manifold, which can be initialized, manipulated, and read out conveniently at room temperature using laser and microwave fields [32]. The spin dependence of the NV center's fluorescence (about 600–800 nm) can be explained by different radiative and nonradiative decay pathways for the $m_S = 0$ and $m_S = \pm1$ (hereinafter referred to as $|0\rangle$ and $|\pm1\rangle$) spin projections. The essential electronic structure of the NV center at nonzero external magnetic field B_z is shown in Fig. 1(a), where radiative and nonradiative transitions can occur between the excited (^3E) and ground (^3A) states, denoted by the solid and dashed arrows, respectively. The nonradiative transitions to metastable singlet states from the excited levels are stronger from the $|\pm1\rangle$ states than from the $|0\rangle$ state; therefore, the NV center shows less fluorescence in the $|\pm1\rangle$ states compared to the $|0\rangle$ state. The solid green arrow indicates the off-resonant excitation by a green laser, which is used to read out the spin state of the NV center. The excitation laser also spin polarizes the NV center into the $|0\rangle$ sublevel by cycling the radiative and nonradiative transitions.

The Hamiltonian for the ground state of the NV center including the coupling to the ^{15}N nucleus ($I = 1/2$) can be written as

$$\mathcal{H}_{\mathrm{NV}} = DS_z^2 + \gamma_e B_z S_z + \gamma_n B_z I_z + A S_z I_z. \tag{1}$$

The zero-field energy splitting between the $|0\rangle$ and $|\pm1\rangle$ spin sublevels is $D = 2.87$ GHz, and the degeneracy between $|\pm1\rangle$ can be lifted by applying an external magnetic field B_z along the symmetry axis of the NV center ([111] crystal axis, we refer to this axis as the z axis). S_z and I_z are the z components of the electronic and nuclear spin operators, $\gamma_e = 28.0\,\mathrm{GHz\,T^{-1}}$ and $\gamma_n = 4.32\,\mathrm{MHz\,T^{-1}}$ are the electronic and nuclear gyromagnetic ratios, and $A = 3.03$ MHz is the hyperfine interaction strength for ^{15}N. The hyperfine coupling results in an additional energy splitting of each ground state, which is undesirable for the observation of SRTs or STIRAP (see the Supplemental Material [33] for more details on the influence of nuclear spin polarization). Fortunately, a high degree of nuclear spin polarization can be achieved by working close to a level anticrossing [34] or by spin polarization transfer schemes [35].

Disregarding the multiple nuclear spin states, the ^3A ground state of an NV center can be described by a V-type system, as shown in Fig. 1(b), where the states $|0\rangle \leftrightarrow |\pm1\rangle$ are dipole coupled and the transition $|-1\rangle \leftrightarrow |+1\rangle$ is dipole forbidden. The transition energies between the $|0\rangle$ and $|-1\rangle$ and $|+1\rangle$ states are ω_- and ω_+, respectively ($\hbar = 1$), and the resonant driving fields are Ω_- and Ω_+. The primary aim of SRTs and STIRAP is to drive a direct transition between states $|-1\rangle \leftrightarrow |+1\rangle$ without or with only a little population transfer to state $|0\rangle$ (indicated by the black dashed arrow). For SRTs this is usually achieved by applying two driving fields detuned by Δ, whereas STIRAP uses adiabatic, partially overlapping pulses. The $\delta_\pm$ labeled detuning in Fig. 1(a) indicates an additional unintentional detuning, which is detrimental for the outcome of both SRTs and STIRAP (see Sec. III C and the Supplemental Material [33]). Briefly summarized, what actually matters is $\Delta\delta = |\delta_+ - \delta_-|$. As for the experiment, the driving fields are first always adjusted to $\delta_\pm = 0$, and then during the measurement $|\delta_\pm| > 0$ can occur for different reasons. In our opinion this is a change in temperature, which leads to a net $\Delta\delta \approx 0$ and a change in external magnetic field, which leads to $\Delta\delta \approx 2|\delta_+|$. Spatial inhomogeneities can be ruled out as a cause of errors in detuning $\delta_\pm$, as we confirmed

to probe only a single NV center by observing the photon statistics (see the Supplemental Material [33])

Figure 1(c) shows the implemented protocol to drive and detect microwave SRTs and STIRAP. First, an $\sim 4\,\mu$s green (520 nm) laser pulse followed by a resonant microwave π_- pulse ($\sim 1\,\mu$s) initializes the system into the $|-1\rangle$ state. To drive SRTs two off-resonant driving fields, $\Omega_{+,\Delta}$ and $\Omega_{-,\Delta}$, each detuned by Δ from the respective resonant dipole transition, ω_+ and ω_- [see Fig. 1(a)], are applied simultaneously for a varying time τ. For STIRAP two resonant Raman control pulses with a Gaussian envelope are applied in an adiabatic and partially overlapping way, where the $|0\rangle \leftrightarrow |+1\rangle$ driving field Ω_+ is applied earlier than the $|0\rangle \leftrightarrow |-1\rangle$ driving field Ω_-. The field amplitudes of the two Raman microwaves are, in either case, carefully adjusted (especially also considering the saturation behavior of the amplifier) to yield a nearly identical Rabi frequency $\Omega_{+,(\Delta)} \approx \Omega_{-,(\Delta)}$.

Subsequent to the (detuned) Raman pulses, the population in each of the three spin states can be read out by either directly reading out the NV fluorescence (the population in $|0\rangle$ is read out) or applying another state-selective resonant microwave π_+ or π_- pulse ($\sim 1\,\mu$s) before reading out the fluorescence (the population in $|+1\rangle$ or $|-1\rangle$ is read out, respectively).

An example of the theoretic dynamic evolution of the three ground states, induced by two detuned SRT microwave pulses or two adiabatic STIRAP pulses, is shown in Fig. 1(d). The dynamics shown here are calculated by unitary time evolution of the incident state vector which starts, as indicated in Fig. 1(a), with a polarized nuclear and electron spin in state $|-1\rangle$. For SRTs we subsequently apply the two-photon Raman microwave (MW) driving field:

$$V(t)_{\mathrm{SRT}} = B_{x,+}\sin[(\omega_+ - \Delta)t] + B_{x,-}\sin[(\omega_- - \Delta)t], \quad (2)$$

where $B_{x,+}$ and $B_{x,-}$ are the magnetic field amplitudes of the applied MW field orthogonal to the NV symmetry axis. For STIRAP the driving field intensities are additionally modulated by

$$f(t)_\pm = e^{-(t-\mu_\pm)^2/2\sigma^2}, \quad (3)$$

which describes a Gaussian distribution with standard deviation σ and maximum value at times μ_+ and μ_- for ω_+ and ω_-, respectively. Hence, the STIRAP driving field can be described by

$$V(t)_{\mathrm{STIRAP}} = B_{x,+}\sin(\omega_+ t)e^{-(t-\mu_+)^2/2\sigma^2} + B_{x,-}\sin(\omega_- t)e^{-(t-\mu_-)^2/2\sigma^2}. \quad (4)$$

With the ground state Hamiltonian of the NV center $\mathcal{H}_{NV}$ [Eq. (1)] and the driving field $V(t)$ [Eq. (2) or Eq. (4)], we can write the system Hamiltonian in the laboratory frame as

$$\mathcal{H}_{\mathrm{NV}}^{\mathrm{Sys}} = \mathcal{H}_{NV} + (\gamma_e S_x + \gamma_n I_x)V(t). \quad (5)$$

From this system Hamiltonian the evolution of the electron spin population in the three sublevels $|0\rangle$, $|-1\rangle$, and $|+1\rangle$ is computed using the Lindblad master equation solver of the QUTIP library [36]. In this solver a dissipation process can be added by a collapse operator. Additional collapse operators can be added to the solver to simulate decoherence.

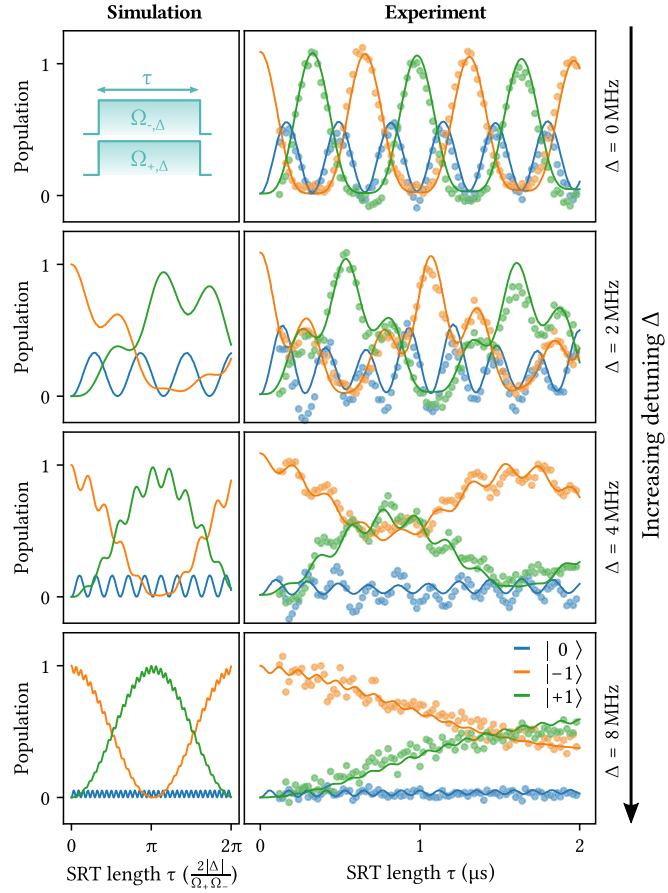

FIG. 2. Simulation (left) and experimental results (right) for SRTs. From top to bottom the detuning of the drive fields is increased from $\Delta = 0$ MHz to $\Delta = 8$ MHz, as indicated on the right. The left column shows the simulated ideal evolution of the three states in units of effective Rabi frequency $\Omega_{\mathrm{SRT}} = \Omega_+\Omega_-/(2|\Delta|)$ up to $\Omega_{\mathrm{SRT}} = 2\pi$ (with $\Omega_{\pm,\Delta} = 2$ MHz). The data points in the right column show the experimentally measured populations of the three ground states $|0\rangle$, $|-1\rangle$, and $|+1\rangle$ (blue, orange, and green, respectively) as a function of the Raman pulse length τ, and the data were used for simultaneous fitting of simulations (solid lines). In the experiment, the Rabi frequency of the two Raman pulses is adjusted to $\Omega_{\pm,\Delta} \approx 2$ MHz.

III. EXPERIMENTAL IMPLEMENTATION

The experiments on SRTs and STIRAP are carried out by observing the spin-dependent fluorescence of a single NV center at room temperature using a home-built confocal microscope. The NV center is hosted in a [111] chemical vapor deposition grown ^{15}N δ-doped diamond substrate (more information on δ doping can be found in [21]) and can be optically excited with a diode laser at 520 nm through a high numerical aperture ($= 1.35$) oil immersion objective. The ^{15}N nuclear spin is polarized into the $m_I = +1/2$ state by a static magnetic field $B_z \approx 381$ G (close to the excited state level anticrossing), applied and precisely aligned along the z axis of the NV center via a permanent magnet. A strong hyperpolarization in $m_I = +1/2$ and good alignment of the magnetic field is verified by a vanishing electron spin resonance line of the nuclear spin state $m_I = -1/2$ (see the Supplemental Material [33] for more information on nuclear spin polarization).

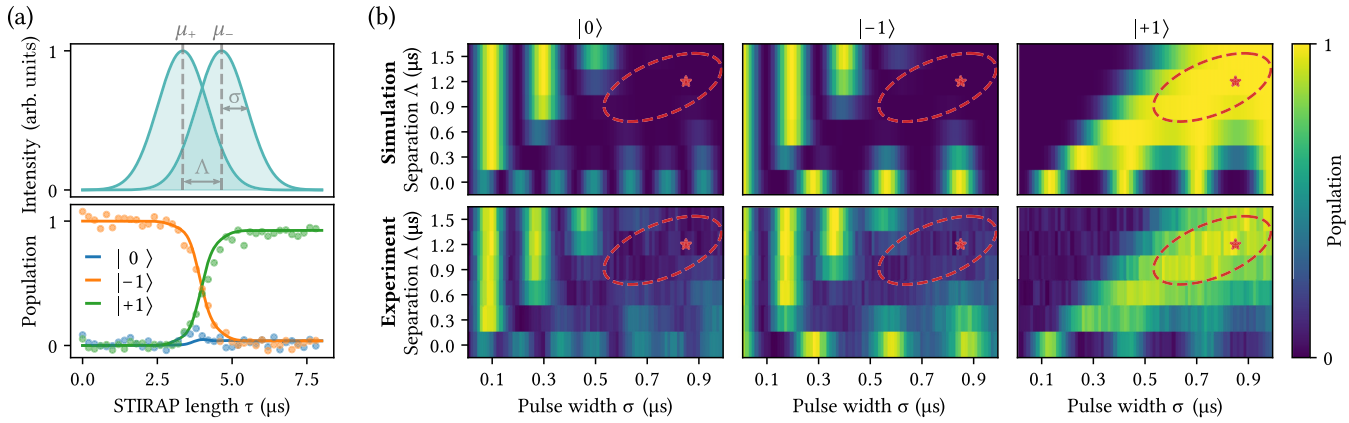

FIG. 3. STIRAP in the ground state of the NV center. (a) The upper plot shows the normalized Gaussian profile of the two resonant STIRAP control fields Ω_- and Ω_+. The Gaussian envelopes have equal width σ and maximum value at times μ_- and μ_+, respectively. The lower plot shows experimental (data points) and simulated (solid lines) values for the population evolution in the NV ground states $|0\rangle$, $|-1\rangle$, and $|+1\rangle$ subject to the above STIRAP fields with maximum Rabi frequency $\Omega_\pm \approx 2\,\mathrm{MHz}$, pulse separation $\Lambda = \mu_- - \mu_+ = 1.2\,\mu\mathrm{s}$, and pulse width $\sigma = 0.85\,\mu\mathrm{s}$. (b) The heat maps show the simulated (top row) and experimentally detected (bottom row) final populations in the three ground states $|0\rangle$ (left), $|-1\rangle$ (middle), and $|+1\rangle$ (right) after STIRAP control, depending on separation Λ and width σ of the Gaussian control pulses. The asterisk marks the values from (a), and the red dashed area marks the broad range in which almost complete STIRAP transfer to $|+1\rangle$ occurs in the simulation as well as in the experiment, thus visualizing the robustness of STIRAP against pulse width errors.

To drive transitions between the ground state sublevels, the two resonant and two off-resonant microwave fields for SRT are generated by analog microwave signal generators and chopped by fast MW switches before being combined. The STIRAP sequence is directly synthesized by an arbitrary wave form generator. All MW fields are amplified and sent to a 50 μm thick copper wire, which is brought in close proximity to the NV center (see the Supplemental Material [33] for more details on the experimental setup). To mitigate random and systematic fluctuations in detected photons and slow drifts, the collection of data points is randomized, and each measurement sequence is additionally corrected for by a reference sequence (see the Supplemental Material [33] for more details on the measurement sequence).

A. Stimulated Raman transitions

In Fig. 2 we show a combination of results from simulations and experiments of SRTs in the NV center. As outlined in Sec. II, two detuned control fields $\Omega_{\pm,\Delta}$ are switched on simultaneously for length τ to drive SRTs, as shown in the upper left corner of Fig. 2.

The left column of Fig. 2 shows the simulated ideal evolution for the population in the three states $|0\rangle$, $|-1\rangle$, and $|+1\rangle$ depending on SRT pulse length without any decoherence mechanisms and unintentional detuning $\delta_\pm = 0\,\mathrm{MHz}$. These calculations show that the population into the $|0\rangle$ state and the effective Raman inversion frequency Ω_{SRT} are decreasing for increasing detuning Δ (note that the detuning Δ changes the scaling of the x axis in the plots). In the limit of large detunings Δ the system can then be, in principle, reduced to a two-level spin system with an effective Rabi frequency for the spin-flip Raman transition of $\Omega_{\mathrm{SRT}} = \Omega_+\Omega_-/(2|\Delta|)$ [37].

The right column of Fig. 2 shows experimental results (data points) and their respective theoretical evolution (solid lines) obtained by simulations. In the experiment, the amplitude of the two detuned Raman pulses is carefully adjusted to drive each of the two transitions with a Rabi frequency $\Omega_\pm \approx 2\,\mathrm{MHz}$, at the respective resonant transitions ω_+ and ω_-. In contrast to the simulations in the left column of Fig. 2, the fits to the data are made considering all three spin states and including decoherence and errors in the amplitude of the two detuned Raman pulses (Rabi frequencies $\Omega_{\pm,\Delta}$) as well as errors in detuning $\delta_\pm$. In the fitting process, simulations of the spin dynamics with varying unintentional detuning $\delta_\pm$ and decoherence are performed, and the obtained data are fitted to the experimental data points for all three spin states simultaneously, where the quality of the fit is evaluated and the parameters are accordingly adapted until the best values are found.

For $\Delta = 0$ three-state Rabi oscillations can be seen in which the population in $|0\rangle$ reaches about 0.5, while at higher detunings the population in $|0\rangle$ is drastically reduced since the system is coherently driven from $|-1\rangle$ to $|+1\rangle$ and back. At higher detuning Δ, a reduction of coherence between $|-1\rangle$ and $|+1\rangle$ can be observed, which among other typical decoherence channels [38] can arise from errors in $\Omega_{\pm,\Delta}$ and $\delta_\pm$ (which in turn can be caused by magnetic field drift, see the Supplemental Material [33]), complicating the experimental implementation of SRTs at higher magnetic fields.

B. Stimulated Raman adiabatic passage

For STIRAP control [28,39,40], the two Raman control pulses are applied adiabatically and partially overlapping to produce a complete population transfer between two quantum states without or with only barely populating a (short-lived) intermediate state. STIRAP has the advantage of being "robust" as it relies on adiabatic change in the rotating-wave approximation Hamiltonian, which makes it less sensitive to variations, e.g., of the control pulse (detuning, duration, shape, area) [28] or, as in our case, changes in the magnetic field strength, which in turn can be caused by mechanical drift of the sample with respect to the employed permanent magnet.

In the top panel of Fig. 3(a) the Gaussian envelope of the two STIRAP control fields used in the experiment and described in Eq. (3) is illustrated. In STIRAP the two pulses are applied in a seemingly *counterintuitive* ordering, which in our case means the $|0\rangle \leftrightarrow |+1\rangle$ driving field Ω_+ is applied first with a peak at μ_+ (even though there is no initial population in state $|0\rangle$ or $|+1\rangle$) and the second driving field Ω_-, resonant to the transition $|0\rangle \leftrightarrow |-1\rangle$ and with a peak at μ_-, is applied subsequently. The separation between the peaks of the two Gaussian envelopes is $\Lambda = \mu_- - \mu_+$, and the two Gaussian pulses are set to the same width and peak amplitude, as well as temporal pulse area and hence integrated Rabi frequency. After a width of $w = 8\sigma$ the amplitude of each microwave field is set to zero both in the numerical simulation and in the experiment.

The bottom panel of Fig. 3(a) shows experimental results for the dynamic evolution (data points) of the three ground states $|0\rangle$, $|-1\rangle$, and $|+1\rangle$ (blue, orange, and green, respectively) of the NV center, after applying the two previously described resonant STIRAP Gaussian-shaped drive fields. For this experiment, the STIRAP sequence was clipped (which means that the amplitude of the drive fields is suddenly set to zero) after time τ, as shown in Fig. 1(b) to visualize the STIRAP transfer dynamics. It can be clearly seen that population transfer from $|-1\rangle$ to $|+1\rangle$ occurs with almost no population in $|0\rangle$, a signature of traditional STIRAP. The experimental results also fit well with theoretically calculated dynamics (see Sec. II) including decoherence (solid line).

In STIRAP the focus lies in the robustness and success of the spin swap; therefore, the six plots arranged in tabular form in Fig. 3(b) show the final population in each of the three ground states, depending on the separation of the two Gaussian control pulses Λ and the standard deviation width σ of the pulses. The three columns represent the final populations in $|0\rangle$, $|-1\rangle$, and $|+1\rangle$, where the top row shows numerically simulated data and the bottom row shows experimental data. For $\Lambda = 0$ one sees, as expected, three-state Rabi oscillations where the population in $|0\rangle$ reaches about 0.5, similar to the value in the SRT experiment. For higher pulse separation Λ the population shows plateaus in both simulation and experimental data where a complete population transfer can occur for a wide range of pulse widths (final populations in $|0\rangle \to 0$, $|-1\rangle \to 0$, and $|+1\rangle \to 1$, red dashed circled areas are a guide for the eye), showing that microwave STIRAP can be a very robust method to drive the spin-forbidden $|-1\rangle \leftrightarrow |+1\rangle$ transition in the ground state of the NV center. The heat maps in Fig. 3(b) can also be used to choose a robust point to perform STIRAP experiments; in this case the asterisks in the heat maps mark the points where the dynamic STIRAP evolution in Fig. 3(a) was recorded, and slight changes in the microwave pulses should have no strong effects on the outcome of the sequence around this point. Furthermore, from the dynamic STIRAP evolution we can infer that almost no population is transferred into $|-1\rangle$ during STIRAP evolution in the marked area.

C. Robustness of SRT and STIRAP

STIRAP also promises to be to more robust to unintentional frequency detuning of the two control pulses $\delta_\pm$ [see Fig. 1(b)], meaning an additional offset to the intentionally detuned SRT pulse frequency or the resonant STIRAP pulse frequency. The effect of this frequency detuning on the outcome of the SRT or STIRAP sequence is presented in Fig. 4, where detuning maps compare the final population in state $|+1\rangle$ with respect to frequency detuning of the two control pulses $\delta_\pm$ for SRT and STIRAP.

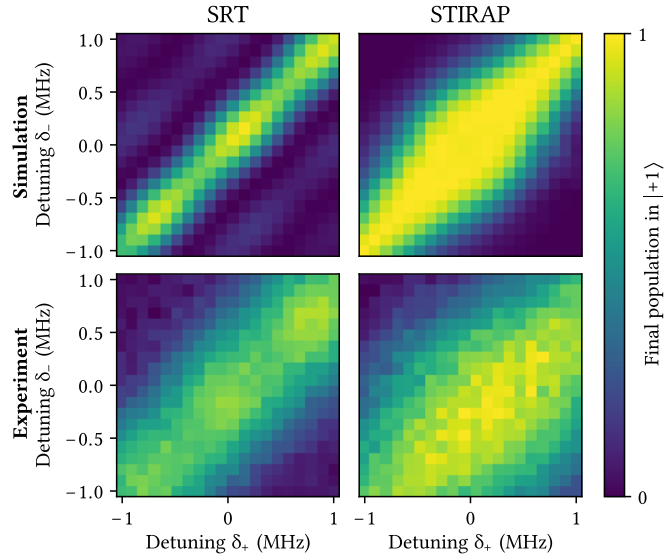

FIG. 4. Comparison of the robustness of SRT and STIRAP against frequency errors. The heat maps represent the final population of the desired state $|+1\rangle$ with SRT (left column) and STIRAP (right column) control depending on an unintentional frequency detuning $\delta_\pm$ of the two control pulses. The top row shows simulation results, and the bottom row shows experimental results. SRTs were chosen with an initial detuning $\Delta = 5\,\text{MHz}$, and STIRAP was chosen with no initial detuning, Gaussian rms width $\sigma = 0.85\,\mu\text{s}$, and pulse separation $\Lambda = 1.2\,\mu\text{s}$. The simulation shows much sharper patterns than the experimental data, which is most likely due to frequency jitter occurring during the acquisition of data. Nevertheless, a strong dependence of SRTs on frequency errors (which can occur due to changes in applied magnetic field, temperature, or drift) and the higher robustness of STIRAP against such errors, i.e., a larger area where spin flip was successful, are apparent.

The top row of Fig. 4 compares the outcome of a simulated SRT and STIRAP sequence in the desired final state $|+1\rangle$. It is evident from these simulations that in the case of SRT a small frequency error ($\delta \ll 1\,\text{MHz}$) already has a strong effect on the outcome of the sequence, whereas STIRAP shows a much higher robustness against frequency changes. The bottom row of Fig. 4 shows the corresponding experimental data. A systematic deviation of the experimental data from the simulation can be observed, which is most likely due to frequency drifts during the acquisition of the data. A two-dimensional (2D) detuning map with $20 \times 20 = 400$ individual data points each integrated for about 0.5–1.0 s usually takes about 5 min for a single acquisition. This is then repeated about 50 times in order to obtain 2D detuning maps with low noise, as can be seen in Fig. 4. However, even in regard to only the data from the first integration the sharp features expected from the simulation cannot be found; therefore, the frequency fluctuations appear to be on a timescale <5 min. However, the data

still confirms that the STIRAP sequence is less sensitive to frequency changes and suffers less from decoherence.

Frequency drifts can occur internal or external to the NV center, meaning either the resonance frequency of the NV itself shifts, one reason for which can be thermally induced lattice strains [41], or the actual magnetic field applied to the NV center changes, e.g., caused by mechanical drifts (see the Supplemental Material [33] for more information on magnetic field drifts). Especially in the case of SRT we can see that drifts of the applied magnetic field (which shifts δ_+ and δ_- in opposite directions) can aggravate the outcome of the sequence drastically. Further evaluation of the influence of the intentional SRT detuning Δ on the robustness can be found in the Supplemental Material [33].

Furthermore, we want to mention that direct transfer from $|-1\rangle$ and $|+1\rangle$, e.g., through STIRAP can be advantageous in systems where spontaneous decay can more likely occur from the intermediate level, which is bypassed. In the NV center, however, dephasing can occur in all three states, $|0\rangle$, $|-1\rangle$, and $|+1\rangle$; therefore, this specific feature of SRTs or STIRAP is not relevant here.

IV. CONCLUSION AND OUTLOOK

Summarizing, we showed the microwave stimulated Raman transitions and stimulated Raman adiabatic passage in the triplet ground state of the NV center. This was achieved either by using a two-photon microwave pulse that simultaneously drives two detuned ground state transitions for SRTs or applying two partially overlapping resonant adiabatic pulses for STIRAP. We elucidated the theoretical framework for SRT and STIRAP ground state spin dynamics and experimentally observed both SRT and STIRAP dynamics, demonstrating the ability to drive the spin-forbidden $m_S = -1$ to $m_S = +1$ transition with almost no population transfer to the $m_S = 0$ level in both cases.

SRTs proved to be technically easier to realize as no adiabatic pulses are required but suffer more from decoherence, especially for higher mean detuning, and also are experimentally more challenging due to high sensitivity to frequency errors, which can, for example, occur from mechanical drifts. STIRAP requires adiabatic pulse shapes, which are technically more demanding to generate, but proved to be more robust to both pulse area deviations and frequency fluctuations and also suffers less from decoherence, hence rendering it simpler to realize experimentally.

The possibility to drive microwave SRT and STIRAP transitions in the ground state of the NV center and thus driving the spin-forbidden transition of the system via microwaves could open up new possibilities for quantum control schemes of the NV center, which could be applied, for example, in future quantum sensing schemes. Furthermore, the microwave STIRAP sequence could be adapted to generate dressed states in the NV center, offering coherence protection.

ACKNOWLEDGMENT

We acknowledge financial support from the Federal Ministry of Education and Research of Germany in the framework of Q.Link.X (Project No. 16KIS0876). The simulations are coded in PYTHON using the QUTIP library [36].

[1] D. D. Awschalom, L. C. Bassett, A. S. Dzurak, E. L. Hu, and J. R. Petta, Quantum spintronics: Engineering and manipulating atom-like spins in semiconductors, Science **339**, 1174 (2013).

[2] M. Shapiro and P. Brumer, Coherent Control of Atomic, Molecular, and Electronic Processes, Adv. At. Mol. Opt. Phys. **42**, 287 (2000).

[3] I. R. Sola, B. Y. Chang, S. A. Malinovskaya, and V. S. Malinovsky, Quantum Control in Multilevel Systems, Adv. At. Mol. Opt. Phys. **67**, 151 (2018).

[4] N. Timoney, I. Baumgart, M. Johanning, A. F. Varón, M. B. Plenio, A. Retzker, and C. Wunderlich, Quantum gates and memory using microwave-dressed states, Nature (London) **476**, 185 (2011).

[5] X. Xu, Z. Wang, C. Duan, P. Huang, P. Wang, Y. Wang, N. Xu, X. Kong, F. Shi, X. Rong, and J. Du, Coherence-Protected Quantum Gate by Continuous Dynamical Decoupling in Diamond, Phys. Rev. Lett. **109**, 070502 (2012).

[6] D. A. Golter, T. K. Baldwin, and H. Wang, Protecting a Solid-State Spin from Decoherence Using Dressed Spin States, Phys. Rev. Lett. **113**, 237601 (2014).

[7] A. Gruber, A. Dräbenstedt, C. Tietz, L. Fleury, J. Wrachtrup, and C. Von Borczyskowski, Scanning confocal optical microscopy and magnetic resonance on single defect centers, Science **276**, 2012 (1997).

[8] L. Rondin, J.-P. Tetienne, T. Hingant, J.-F. Roch, P. Maletinsky, and V. Jacques, Magnetometry with nitrogen-vacancy defects in diamond, Rep. Prog. Phys. **77**, 056503 (2014).

[9] F. Jelezko, T. Gaebel, I. Popa, A. Gruber, and J. Wrachtrup, Observation of Coherent Oscillations in a Single Electron Spin, Phys. Rev. Lett. **92**, 076401 (2004).

[10] J. R. Maze, P. L. Stanwix, J. S. Hodges, S. Hong, J. M. Taylor, P. Cappellaro, L. Jiang, M. V. G. Dutt, E. Togan, A. S. Zibrov, A. Yacoby, R. L. Walsworth, and M. D. Lukin, Nanoscale magnetic sensing with an individual electronic spin in diamond, Nature (London) **455**, 644 (2008).

[11] G. Balasubramanian, I. Y. Chan, R. Kolesov, M. Al-Hmoud, J. Tisler, C. Shin, C. Kim, A. Wojcik, P. R. Hemmer, A. Krueger, T. Hanke, A. Leitenstorfer, R. Bratschitsch, F. Jelezko, and J. Wrachtrup, Nanoscale imaging magnetometry with diamond spins under ambient conditions, Nature (London) **455**, 648 (2008).

[12] J. M. Taylor, P. Cappellaro, L. Childress, L. Jiang, D. Budker, P. R. Hemmer, A. Yacoby, R. Walsworth, and M. D. Lukin, High-sensitivity diamond magnetometer with nanoscale resolution, Nat. Phys. **4**, 810 (2008).

[13] X. Rong, M. Wang, J. Geng, X. Qin, M. Guo, M. Jiao, Y. Xie, P. Wang, P. Huang, F. Shi, Y.-F. Cai, C. Zou, and J. Du, Searching for an exotic spin-dependent interaction with a single electron-spin quantum sensor, Nat. Commun. **9**, 1 (2018).

[14] P. Rembold, N. Oshnik, M. M. Müller, S. Montangero, T. Calarco, and E. Neu, Introduction to quantum optimal control

for quantum sensing with nitrogen-vacancy centers in diamond, AVS Quantum Sci. **2**, 024701 (2020).

[15] M. Fujiwara, S. Sun, A. Dohms, Y. Nishimura, K. Suto, Y. Takezawa, K. Oshimi, L. Zhao, N. Sadzak, Y. Umehara, Y. Teki, N. Komatsu, O. Benson, Y. Shikano, and E. Kage-Nakadai, Real-time nanodiamond thermometry probing in vivo thermogenic responses, Sci. Adv. **6** eaba9636 (2020).

[16] J. Wrachtrup and F. Jelezko, Processing quantum information in diamond, J. Phys.: Condens. Matter **18**, S807 (2006).

[17] J. Cai, A. Retzker, F. Jelezko, and M. B. Plenio, A large-scale quantum simulator on a diamond surface at room temperature, Nat. Phys. **9**, 168 (2013).

[18] F. Dolde, I. Jakobi, B. Naydenov, N. Zhao, S. Pezzagna, C. Trautmann, J. Meijer, P. Neumann, F. Jelezko, and J. Wrachtrup, Room-temperature entanglement between single defect spins in diamond, Nat. Phys. **9**, 139 (2013).

[19] P. Neumann, N. Mizuochi, F. Rempp, P. Hemmer, H. Watanabe, S. Yamasaki, V. Jacques, T. Gaebel, F. Jelezko, and J. Wrachtrup, Multipartite entanglement among single spins in diamond, Science **320**, 1326 (2008).

[20] C. Zu, W.-B. Wang, L. He, W.-G. Zhang, C.-Y. Dai, F. Wang, and L.-M. Duan, Experimental realization of universal geometric quantum gates with solid-state spins, Nature (London) **514**, 72 (2014).

[21] K. Ohno, F. J. Heremans, L. C. Bassett, B. A. Myers, D. M. Toyli, A. C. Bleszynski Jayich, C. J. Palmstrøm, and D. D. Awschalom, Engineering shallow spins in diamond with nitrogen delta-doping, Appl. Phys. Lett. **101**, 082413 (2012).

[22] H. J. Mamin, M. H. Sherwood, M. Kim, C. T. Rettner, K. Ohno, D. D. Awschalom, and D. Rugar, Multipulse Double-Quantum Magnetometry with Near-Surface Nitrogen-Vacancy Centers, Phys. Rev. Lett. **113**, 030803 (2014).

[23] K. Fang, V. M. Acosta, C. Santori, Z. Huang, K. M. Itoh, H. Watanabe, S. Shikata, and R. G. Beausoleil, High-Sensitivity Magnetometry Based on Quantum Beats in Diamond Nitrogen-Vacancy Centers, Phys. Rev. Lett. **110**, 130802 (2013).

[24] J. F. Barry, J. M. Schloss, E. Bauch, M. J. Turner, C. A. Hart, L. M. Pham, and R. L. Walsworth, Sensitivity optimization for NV-diamond magnetometry, Rev. Mod. Phys. **92**, 015004 (2020).

[25] C. Ospelkaus, U. Warring, Y. Colombe, K. R. Brown, J. M. Amini, D. Leibfried, and D. J. Wineland, Microwave quantum logic gates for trapped ions, Nature (London) **476**, 181 (2011).

[26] P. Scarlino, D. J. van Woerkom, U. C. Mendes, J. V. Koski, A. J. Landig, C. K. Andersen, S. Gasparinetti, C. Reichl, W. Wegscheider, K. Ensslin, T. Ihn, A. Blais, and A. Wallraff, Coherent microwave-photon-mediated coupling between a semiconductor and a superconducting qubit, Nat. Commun. **10**, 3011 (2019).

[27] B. Pingault, D. D. Jarausch, C. Hepp, L. Klintberg, J. N. Becker, M. Markham, C. Becher, and M. Atatüre, Coherent control of the silicon-vacancy spin in diamond, Nat. Commun. **8**, 1 (2017).

[28] B. W. Shore, Picturing stimulated Raman adiabatic passage: A STIRAP tutorial, Adv. Opt. Photonics **9**, 563 (2017).

[29] D. A. Golter and H. Wang, Optically Driven Rabi Oscillations and Adiabatic Passage of Single Electron Spins in Diamond, Phys. Rev. Lett. **112**, 116403 (2014).

[30] J. Tian, T. Du, Y. Liu, H. Liu, F. Jin, R. S. Said, and J. Cai, Optimal quantum optical control of spin in diamond, Phys. Rev. A **100**, 012110 (2019).

[31] Z. Shu, Y. Liu, Q. Cao, P. Yang, S. Zhang, M. B. Plenio, F. Jelezko, and J. Cai, Observation of Floquet Raman Transition in a Driven Solid-State Spin System, Phys. Rev. Lett. **121**, 210501 (2018).

[32] M. W. Doherty, N. B. Manson, P. Delaney, F. Jelezko, J. Wrachtrup, and L. C. Hollenberg, The nitrogen-vacancy colour centre in diamond, Phys. Rep. **528**, 1 (2013).

[33] See Supplemental Material at http://link.aps.org/supplemental/10.1103/PhysRevB.104.035201 for further details on the experimental setup, measurement sequence, polarization of the nuclear spin, and sensitivity to fluctuations.

[34] V. Jacques, P. Neumann, J. Beck, M. Markham, D. Twitchen, J. Meijer, F. Kaiser, G. Balasubramanian, F. Jelezko, and J. Wrachtrup, Dynamic Polarization of Single Nuclear Spins by Optical Pumping of Nitrogen-Vacancy Color Centers in Diamond at Room Temperature, Phys. Rev. Lett. **102**, 057403 (2009).

[35] D. Pagliero, A. Laraoui, J. D. Henshaw, and C. A. Meriles, Recursive polarization of nuclear spins in diamond at arbitrary magnetic fields, Appl. Phys. Lett. **105**, 242402 (2014).

[36] J. R. Johansson, P. D. Nation, and F. Nori, QuTiP 2: A Python framework for the dynamics of open quantum systems, Comput. Phys. Commun. **184**, 1234 (2013).

[37] T. M. Sweeney, C. Phelps, and H. Wang, Quantum control of electron spins in the two-dimensional electron gas of a CdTe quantum well with a pair of Raman-resonant phase-locked laser pulses, Phys. Rev. B **84**, 075321 (2011).

[38] S. Ajisaka and Y. B. Band, Decoherence of three-level systems: Application to nitrogen-vacancy centers in diamond near a surface, Phys. Rev. B **94**, 134107 (2016).

[39] U. Gaubatz, P. Rudecki, S. Schiemann, and K. Bergmann, Population transfer between molecular vibrational levels by stimulated Raman scattering with partially overlapping laser-fields. A new concept and experimental results, J. Chem. Phys. **92**, 5363 (1990).

[40] K. Bergmann, H. Theuer, and B. W. Shore, Coherent population transfer among quantum states of atoms and molecules, Rev. Mod. Phys. **70**, 1003 (1998).

[41] V. M. Acosta, E. Bauch, M. P. Ledbetter, A. Waxman, L.-S. Bouchard, and D. Budker, Temperature Dependence of the Nitrogen-Vacancy Magnetic Resonance in Diamond, Phys. Rev. Lett. **104**, 070801 (2010).